JOURNAL OF GEOPHYSICAL RESEARCH, VOL. 117, A09228, doi:10.1029/2012JA017990, 2012

Rotational modulation and local time dependence of Saturn's infrared H_3^+ auroral intensity

S. V. Badman,[1] D. J. Andrews,[2] S. W. H. Cowley,[3] L. Lamy,[4] G. Provan,[3] C. Tao,[1]
S. Kasahara,[1] T. Kimura,[1] M. Fujimoto,[1] H. Melin,[3] T. Stallard,[3] R. H. Brown,[5]
and K. H. Baines[6]

Received 1 June 2012; revised 16 August 2012; accepted 16 August 2012; published 27 September 2012.

[1] Planetary auroral emissions reveal the configuration of magnetospheric field-aligned current systems. In this study, Cassini Visual and Infrared Mapping Spectrometer (VIMS) observations of Saturn's pre-equinox infrared H_3^+ aurorae were analysed to show (a) rotational modulation of the auroral intensity in both hemispheres and (b) a significant local time dependence of the emitted intensity. The emission intensity is modulated by the 'planetary period' rotation of auroral current systems in each hemisphere. The northern auroral intensity also displays a lesser anti-phase dependence on the southern rotating current system, indicating that part of the southern current system closes in the northern hemisphere. The southern hemisphere aurorae were most intense in the post-dawn sector, in agreement with some past measurements of auroral field-aligned currents, UV aurora and SKR emitted power. A corresponding investigation of the northern hemisphere auroral intensity reveals a broader dawn-noon enhancement, possibly due to the interaction of the southern rotating current system with that of the north. The auroral intensity was reduced around dusk and post-midnight in both hemispheres. These observations can be explained by the interaction of a rotating field-aligned current system in each hemisphere with one fixed in local time, which is related to the solar wind interaction with magnetospheric field lines.

Citation: Badman, S. V., et al. (2012), Rotational modulation and local time dependence of Saturn's infrared H_3^+ auroral intensity, *J. Geophys. Res.*, *117*, A09228, doi:10.1029/2012JA017990.

1. Introduction

[2] The Pioneer and Voyager spacecraft first detected powerful bursts of kilometric radiation from Saturn's auroral regions, the modulation of which was supposed to represent the rotation of the planet's interior [*Kaiser et al.*, 1980; *Desch and Kaiser*, 1981]. Since then, measurements made by the Ulysses and Cassini spacecraft have revealed that the Saturn Kilometric Radiation (SKR) emission periodicity varies on much shorter timescales than can be explained by changes in the planetary rotation rate [*Galopeau and Lecacheux*, 2000; *Kurth et al.*, 2007], and that the emissions from the northern and southern hemispheres have their own independent emission periods [*Gurnett et al.*, 2009; *Lamy*, 2011]. Additionally, 'planetary-period' modulations have been identified in many other magnetospheric phenomena, such as magnetic field perturbations [e.g., *Espinosa and Dougherty*, 2000], charged particle and energetic neutral atom populations [e.g., *Carbary et al.*, 2009], and ultraviolet (UV) auroral emissions [e.g., *Nichols et al.*, 2010a]. The source of this oscillatory behavior is currently a subject of intensive research, as introduced for example in the review by *Mitchell et al.* [2009].

[3] Detailed analysis of the magnetic field oscillations has led to the suggestion that they are signatures of two independent auroral current systems that rotate with different periods in each hemisphere [*Andrews et al.*, 2010; *Southwood*, 2011]. These field-aligned currents are directed across the pole at high-latitudes, i.e. field-aligned downward into the ionosphere on one side of the pole, field-aligned upward from the ionosphere on the other side of the pole, and partially closing in the equatorial plane of the outer magnetosphere, as illustrated in Figures 1c and 1d (reproduced from Figure 9 in *Andrews et al.* [2010]). The field perturbations at high latitudes take the form of planet-centered transverse rotating dipoles in each hemisphere, which are produced by the rotating external current system [*Provan et al.*, 2009]. The near-equatorial field perturbations take the form of quasi-uniform rotating fields aligned with the effective dipoles in the equatorial

---

[1] JAXA Institute of Space and Astronautical Science, Kanagawa, Japan.
[2] Swedish Institute for Space Physics, Uppsala, Sweden.
[3] Department of Physics and Astronomy, University of Leicester, Leicester, UK.
[4] Observatoire de Paris, Meudon, France.
[5] Lunar and Planetary Laboratory, University of Arizona, Tucson, Arizona, USA.
[6] SSEC, University of Wisconsin-Madison, Madison, Wisconsin, USA.

Corresponding author: S. V. Badman, JAXA Institute of Space and Astronautical Science 3-1-1 Yoshinodai, Chuo-ku, Sagamihara, Kanagawa 252-5210, Japan. (s.badman@stp.isas.jaxa.jp)

0148-0227/12/2012JA017990

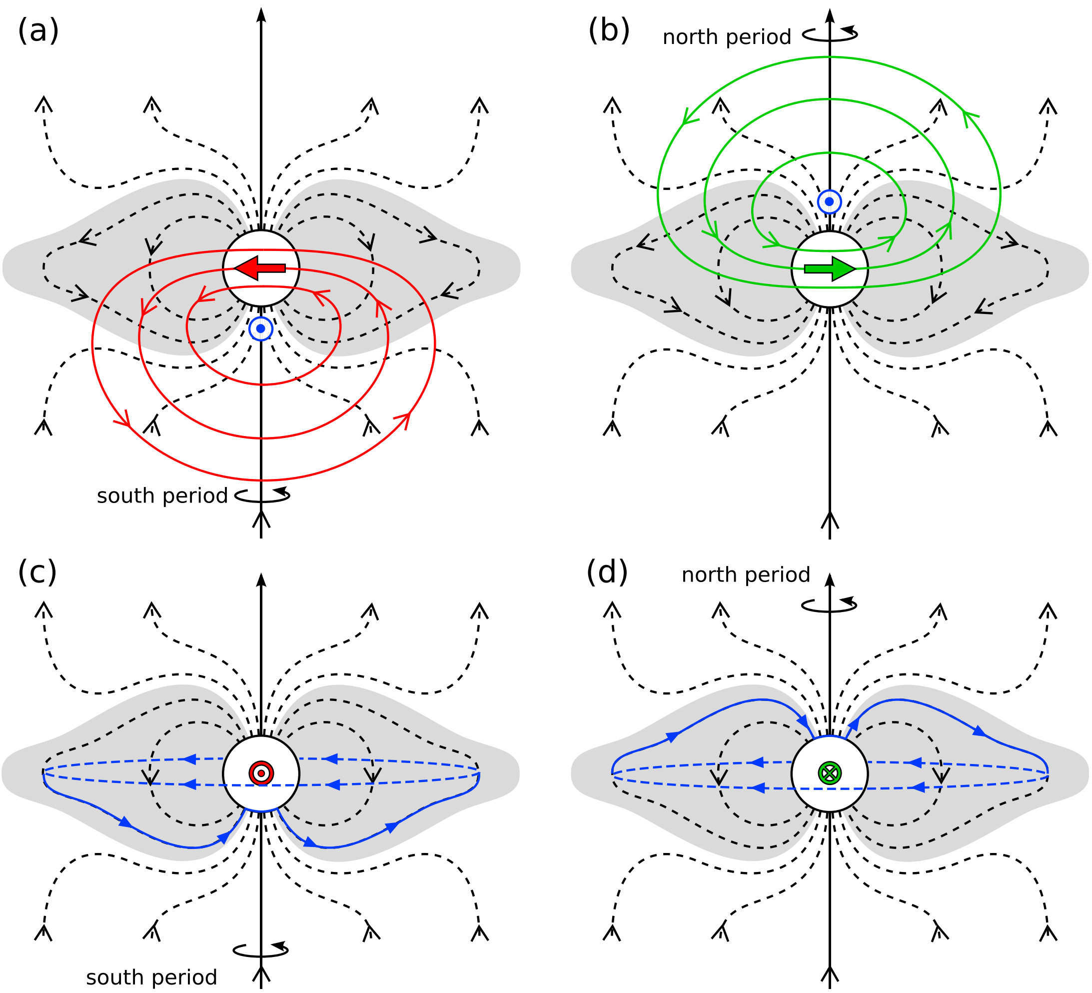

Figure 1. Schematic illustrating the oscillatory perturbation fields and field-aligned current systems. The black lines indicate the magnetospheric field lines in the closed (grey) and open (unshaded) field regions. The perturbation fields at a given instant are shown by (a) the red lines for the southern hemisphere and (b) the green lines for the northern hemisphere. The blue lines in Figures 1c and 1d show the corresponding field-aligned currents in the southern and northern hemispheres, respectively. Reproduced from *Andrews et al.* [2010].

plane, combined with north-south fields, resulting in arched loops [*Andrews et al.*, 2008]. The perturbation fields are also illustrated by the red and green lines in Figures 1a and 1b for the southern and northern hemispheres, respectively.

[4] Upward directed field-aligned currents are important for the generation of aurora at different wavelengths via the downward motion of electrons into the atmosphere. The rotating field-aligned current systems can thus influence the auroral intensity at different local times. The SKR emissions themselves are observed to be most powerful when the rotating upward current passes through the dawn sector [*Lamy et al.*, 2009; *Andrews et al.*, 2010]. Evidence of quasiperiodic intensification has also been identified in the UV aurora, which brightens in the dawn sector in each hemisphere at the corresponding SKR maxima [*Sandel et al.*, 1982; *Nichols et al.*, 2010a]. *Nichols et al.* [2010a] also found a lesser anti-phase effect in the UV emissions at dusk, consistent with a rotating modulation of the auroral intensity.

[5] While investigation to date of oscillatory phenomena in Saturn's aurorae has used UV auroral images [*Nichols et al.*, 2008, 2010a, 2010b], recent analyses of observations by the Cassini Visual and Infrared Mapping Spectrometer (VIMS) [*Brown et al.*, 2004] have shown Saturn's main IR H_3^+ auroral emissions to be co-located with those in the UV and thus driven by the same field-aligned current system [*Badman et al.*, 2011a; *Melin et al.*, 2011]. To generate IR H_3^+ emissions, incident auroral electrons ionize atmospheric H_2 to form H_2^+, which then reacts with H_2 to produce the H_3^+ ionized molecule. Ro-vibrational transitions of the H_3^+ molecule produce the IR auroral emissions [*Drossart et al.*, 1989].

[6] Saturn's H_3^+ emissions are strongly dependent on the atmospheric temperature and the incident auroral electron energy and flux [*Tao et al.*, 2011]. The maximum H_3^+ auroral intensity is expected to occur where the auroral electron flux is maximum i.e. in the regions of maximum upward field-aligned current, and from precipitating electrons with energies up to ~10 keV [*Tao et al.*, 2011]. Auroral currents are important sources of Joule heating in the atmosphere [*Cowley et al.*, 2004a; *Galand et al.*, 2011], therefore a further enhancement of the H_3^+ emission in these regions is expected,

associated with the local temperature increase resulting from Joule heating.

[7] In this study we investigate for the first time how the intensity of Saturn's IR H_3^+ aurora is modulated by local time (LT) and the rotating field-aligned current system described above. The VIMS instrument is capable of higher spatial and temporal resolution than ground-based IR observations, and has observed from a high latitude vantage point, and thus provides a unique opportunity to analyze these characteristics.

2. Auroral Data

[8] This study employs 111 observations of Saturn's H_3^+ aurora acquired by Cassini VIMS during October 2006 to February 2009. Of these, 33 were observations of the southern aurorae and 78 were observations of the northern aurorae. VIMS acquires a full IR wavelength spectrum (0.85–5.1 μm) at each pixel position in its field of view (FOV) in turn, where 1 pixel = 0.5 × 0.5 mrad and the maximum FOV is 64 × 64 pixels. The total time required to build up a 2-D image was typically tens of minutes for the observations used in this study. The data were projected onto a 1° × 1° planetocentric polar grid using an estimated peak emission height of 1100 km above the 1 bar reference spheroid [*Stallard et al.*, 2012]. The emission intensities used here were determined from multiple wavelength bins containing R-branch H_3^+ emission lines around 3.6 μm, and include a simple correction for line-of-sight intensity enhancements, following the method described by *Badman et al.* [2011b].

[9] For each VIMS observation, the intensities were averaged over sections 1° in latitude × 1 h in local time (LT). In each LT section the maximum intensity was then found between the colatitude limits of 10°–25°. These limits contain the typical location of Saturn's main IR auroral emissions [*Badman et al.*, 2011a, 2011b]. Each image covered a different area of the auroral region depending on the VIMS FOV. Only the maximum intensities from sectors which extended from the pole to auroral latitudes, i.e. to at least 14° colatitude (a threshold determined from examination of the images), were included.

3. Magnetic Field Phase Model

[10] We use the phase model of the magnetic field perturbations described by *Andrews et al.* [2012]. This model reproduces the azimuthal rotation of the equatorial quasi-uniform and polar quasi-dipolar fields described above, using a simple rotating sinusoid separately for each hemisphere. Considering first the southern hemisphere, the phase system is defined such that at time, *t*, the direction of the fields points to azimuth $\Phi_{M,S}$ (t), where azimuth increases duskward from noon. The azimuthal direction of the fields projected onto the polar ionosphere of the planet at this arbitrary time, t, is indicated by the red arrow in Figure 2a. The view is looking down through the planet onto the pole with noon to the bottom and dawn to the left. It follows from Figure 1 that the maximum upward field-aligned current in the southern hemisphere occurs at the azimuth where the southern-period equatorial azimuthal perturbation field has its minimum value, which is 90° of azimuth ahead of $\Phi_{M,S}$ (t) [*Andrews et al.*, 2010]. This azimuthal location of the maximum upward field-aligned current is indicated by the blue line in Figure 2a.

[11] Likewise, it also follows from Figure 1 that the maximum upward field-aligned current in the northern hemisphere occurs at the azimuth where the northern-period equatorial azimuthal perturbation field has its maximum value, which is 90° of azimuth behind $\Phi_{M,N}$ (t) [*Andrews et al.*, 2010]. The direction of the rotating fields and the location of the maximum upward field-aligned current at an arbitrary time, t, are illustrated in Figure 2b for the northern hemisphere. The northern and southern current systems rotate with different periods so that the southern and northern effective dipoles do not usually point in the same direction, as exemplified in Figures 2a and 2b.

[12] *Andrews et al.* [2012] compared their magnetic phase systems to the northern and southern SKR phase systems derived by *Lamy* [2011]. The SKR phase systems were determined from examination of the SKR peak emission and are referenced to maximum SKR emission at phase $\Phi_{SKR,N/S} = 360n°$ for integer values of *n* in each hemisphere independently. The northern hemisphere magnetic and SKR phase systems were found to be approximately equal to each other such that at northern SKR maximum, $\Phi_{M,N}(t) \approx \Phi_{SKR,N}(t) = 0°$ (to modulo 360°). At this time, the maximum upward field-aligned current region from the magnetic model is located at dawn, i.e. at azimuth $\phi = -90°$, as shown in Figure 2d.

[13] For the southern hemisphere, *Andrews et al.* [2012] determined that $\Phi_{M,S}(t) \approx \Phi_{SKR,S}(t) - 150°$ in the pre-equinox interval appropriate to the VIMS images employed in this study. Therefore, at southern SKR maximum, when $\Phi_{SKR,S} = 0°$, $\Phi_{M,S}(t) \approx -150°$. The maximum upward field-aligned current in the southern hemisphere is then located at azimuth $\phi = \Phi_{M,S}(t) + 90° \approx -60°$. Similarly to the northern hemisphere, this corresponds to a local time of 08 LT, i.e. post-dawn. This orientation is illustrated in Figure 2c. In the southern hemisphere the maximum SKR emitted power is observed to come from an LT sector of width ~8 LT, centered on 08 LT [*Lamy et al.*, 2009; *Lamy*, 2011], indicated by the grey shaded region in Figure 2c.

4. Example VIMS Observations

[14] Before presenting the results obtained from analysis of all auroral images, we first show in Figure 3 an example sequence of VIMS observations, which cover most of a planetary rotation with a good view of the auroral region. This sequence of six observations was acquired on 10 November 2006 (day of year 314) in the manner described in Section 2. In Figure 3 the observations are projected at 0.5° × 0.5° resolution. The time at the middle of each observation is labeled on each panel. The total accumulation time was 50–70 min for each observation. The yellow grid marks latitudes at intervals of 10° and the noon-midnight and dawn-dusk meridians. The northern magnetic phase at the center time of each observation is also labeled on each panel. The solid yellow line marks the corresponding azimuth of the modelled maximum upward field-aligned current, which rotates at the defined northern hemisphere period and is referenced to 6 LT at $\Phi_{M,N} = 0°$. (This is equivalent to the blue lines illustrating the azimuthal location of the maximum upward field-aligned current in Figures 2b and 2d.)

[15] This sequence begins with the image centered on 1104 UT, when $\Phi_{M,N} = 161°$ i.e. when the maximum upward current region was expected to lie near dusk, and close to

(a) South at arbitrary time, t

(b) North at arbitrary time, t

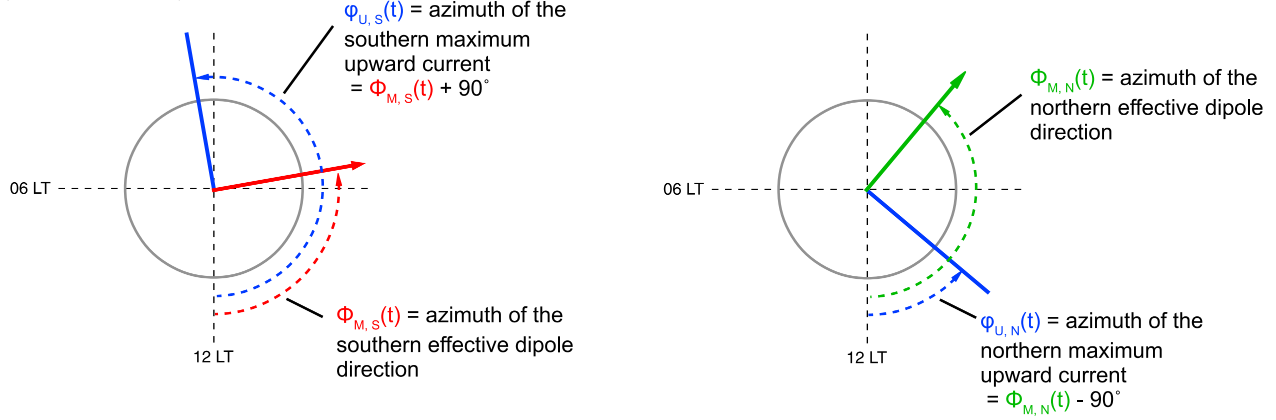

(c) South at time of southern SKR maximum, $\Phi_{SKR,S}$ (t) = 360n°

(d) North at time of northern SKR maximum, $\Phi_{SKR,N}$ (t) = 360n°

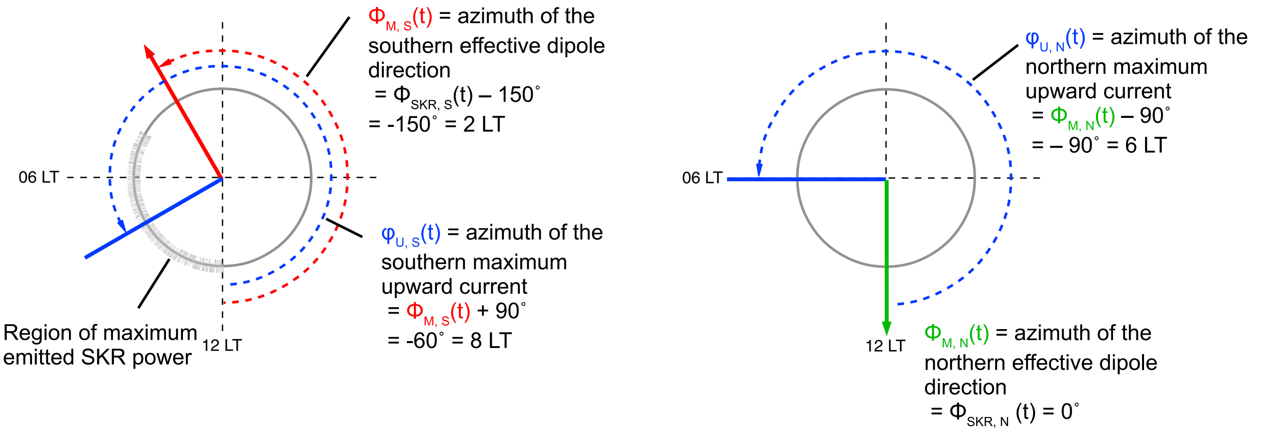

Figure 2. Schematic illustrating the definition of the magnetic phase systems and the relative location of the maximum upward field-aligned current region in the (a) southern and (b) northern hemisphere ionospheres at an arbitrary time, t. These are views looking down onto the pole of the planet with local noon at the bottom, dawn to the left, and dusk to the right. Azimuth is defined as increasing duskward from noon. The colors of the lines correspond to those used in Figure 1, i.e., the red arrow represents the direction of the southern effective dipole, the green arrow represents the direction of the northern effective dipole, and the blue lines indicate the azimuthal location of the maximum upward field-aligned current in both hemispheres. Figures 2c and 2d illustrate the azimuthal location of the effective dipoles and upward field-aligned currents at times of southern and northern SKR maximum emission, respectively.

when a minimum in SKR emission was expected. Figure 3a shows that the IR aurora were relatively dim at this time. Over the next five hours (equivalent to approximately 180° phase) the emissions intensified overall, with a narrow arc becoming apparent in Figures 3b–3d. In the subsequent image e, the most intense IR emissions of the sequence were observed in the post-dawn sector at 1730 UT, $\Phi_{M,N}$ = 20°. These emissions occurred very close to the position of the modelled maximum upward current indicated by the rotating reference axis (yellow line). In the final image the most intense region was located closer to noon and had dimmed slightly.

[16] In Figure 3g, Cassini Radio and Plasma Wave Science (RPWS) [*Gurnett et al.*, 2004] measurements of the SKR emitted flux density on 10 November 2006 are shown in a frequency-time spectrogram. The SKR emissions are the prominent bursts at 100 s of kHz. The vertical dashed lines indicate the times of expected SKR maxima from the model ($\Phi_{M,N}(t) \approx \Phi_{SKR,N}(t) = 0°$), and the labeled arrows at the top mark the times of the images. Panel (h) shows the circular polarization of the waves. The predominance of the white coloring in this panel indicates that most of the detected SKR was RH-polarized, meaning it was emitted from the northern hemisphere, the same as the IR emission observed.

[17] Images (a)–(c) occurred when the SKR emissions were quiet, while (e) and (f) occurred during a regular burst of SKR emission from the northern hemisphere. These were the images displaying the brightest IR emission, showing that the auroral IR and SKR intensities were correlated, and that in this case they maximized at close to the magnetic phase value ($\Phi_{M,N} \sim 0°$) expected from the model. In accordance with this, the most intense IR emissions were observed on the dawnside.

[18] In the following sections the average LT and magnetic phase dependence of Saturn's H_3^+ aurora are determined and

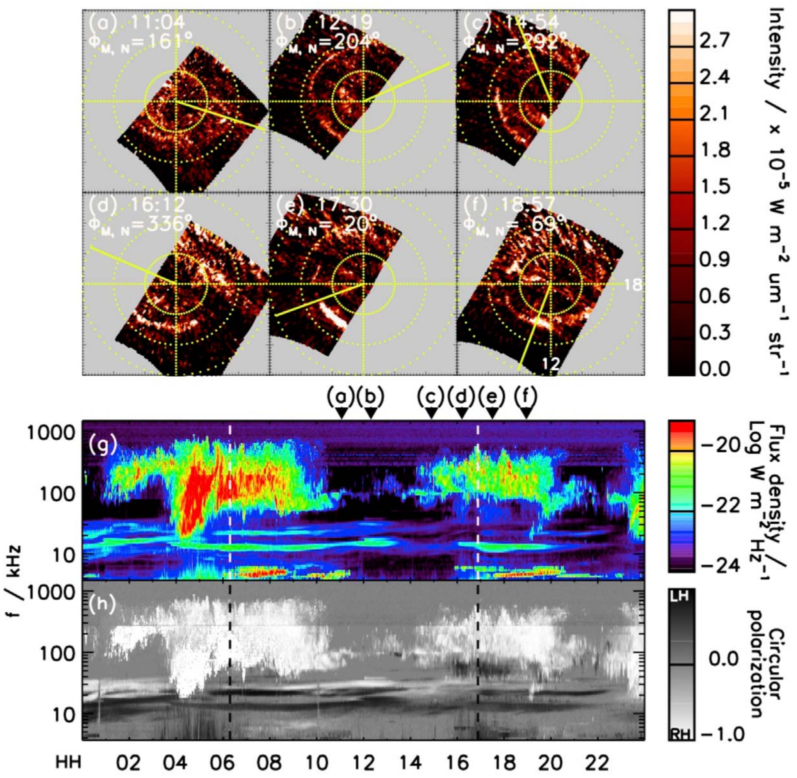

Figure 3. Cassini observations of Saturn's IR aurora and SKR emission on 2006-314. (a)–(f) VIMS observations of the northern IR H_3^+ aurora. The data are projected onto a 0.5° × 0.5° planetocentric grid at 1100 km above the 1-bar reference spheroid, with local noon at the bottom and dusk to the right. The yellow grid marks latitudes at intervals of 10° and the noon-midnight and dawn-dusk meridians. The solid yellow line indicates the location of the expected maximum upward field-aligned current, referenced to 6 LT at $\Phi_{M,N} = 0°$. (g) Cassini RPWS observations of SKR flux density on 2006-314 normalized to 1 AU. The times of images Figures 3a–3f are indicated at the top of the panel. (h) Circular polarization of the waves detected by RPWS, where white indicates right-handed emission originating from the northern hemisphere. The vertical dashed lines mark the times of maximum SKR emission from the northern hemisphere, i.e., $\Phi_{M,N}(t) \approx \Phi_{SKR,N}(t) = 0°$.

compared to the model field-aligned current and observed SKR behavior.

5. Results

[19] The magnetic phase at the center time of each VIMS image integration was determined from the *Andrews et al.* [2012] model. The maximum auroral intensities as functions of LT were determined for each image, as described in Section 2, and then averaged together over 72°-wide bins of magnetic phase. The width of the phase bins encompasses the change in phase that occurs under the longest image accumulation times (~70 min ≈ 40° phase). The average intensities are plotted as functions of LT and magnetic phase for the southern and northern hemispheres in Figure 4.

5.1. Local Time Dependence

[20] Considering first the local time dependence of the intensities in the southern hemisphere, the line plot in the upper panel of Figure 4a shows the average peak intensity distribution across local time, derived from all southern images. The error bars indicate the standard error of the average intensity in each LT bin. This distribution shows a clear peak in the dawn sector with a maximum at 8–9 LT. The average intensity was minimum around dusk (17–19 LT) and increased again pre-midnight.

[21] The intensity distribution across LT in the northern hemisphere, shown in the upper panel of Figure 4b, also reveals a strong, broad peak in the dawn–noon sector. In this case, the maximum intensities were found at 8–12 LT. The intensity distribution decreased post-noon to a local minimum at 16–17 LT, and then increased again post-dusk. The minimum intensity was found in the early morning sector: 2–3 LT. The overall weaker IR emission from the north compared to the south has been attributed by *Badman et al.* [2011b] to the differences in ionospheric conductivity during the pre-equinox interval studied here.

5.2. Magnetic Phase Dependence

[22] The color spectrograms in Figures 4a and 4b show the average peak H_3^+ intensity as a function of LT and

(a) SOUTH

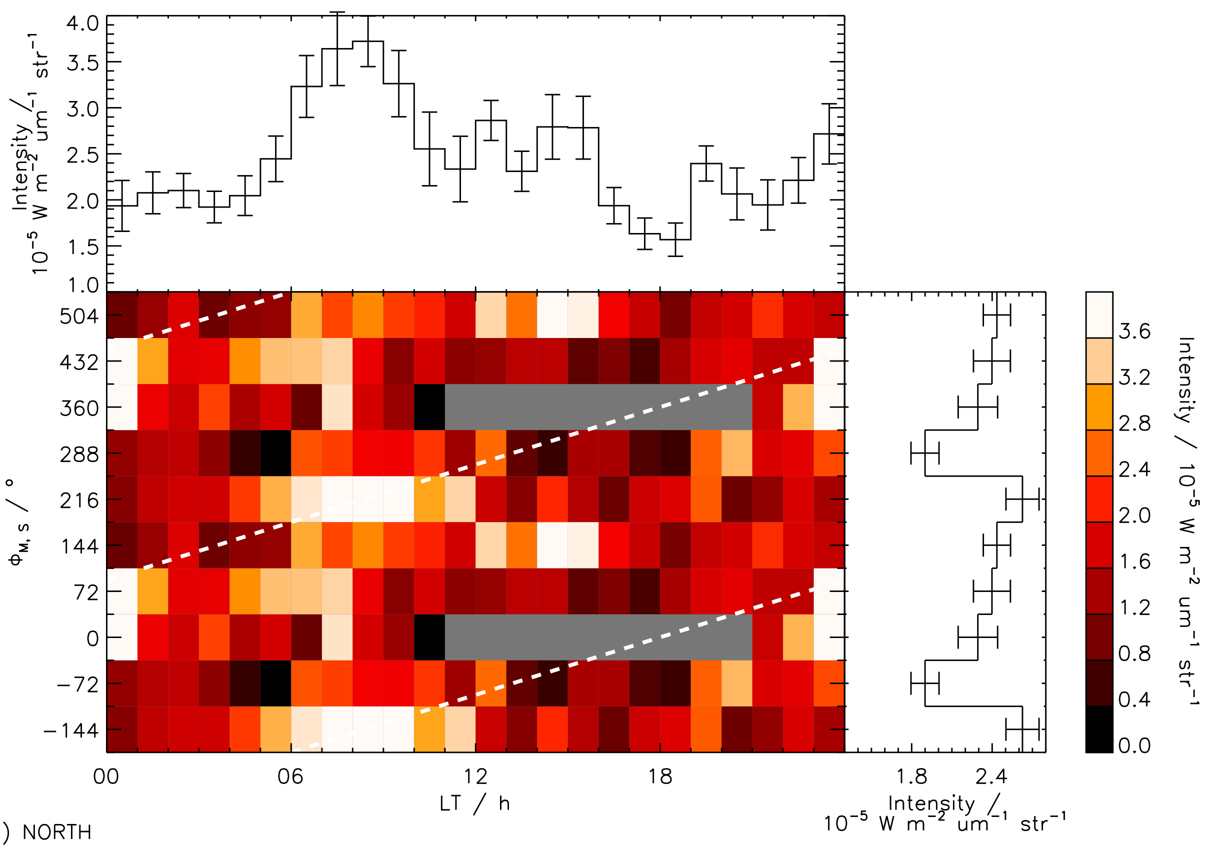

(b) NORTH

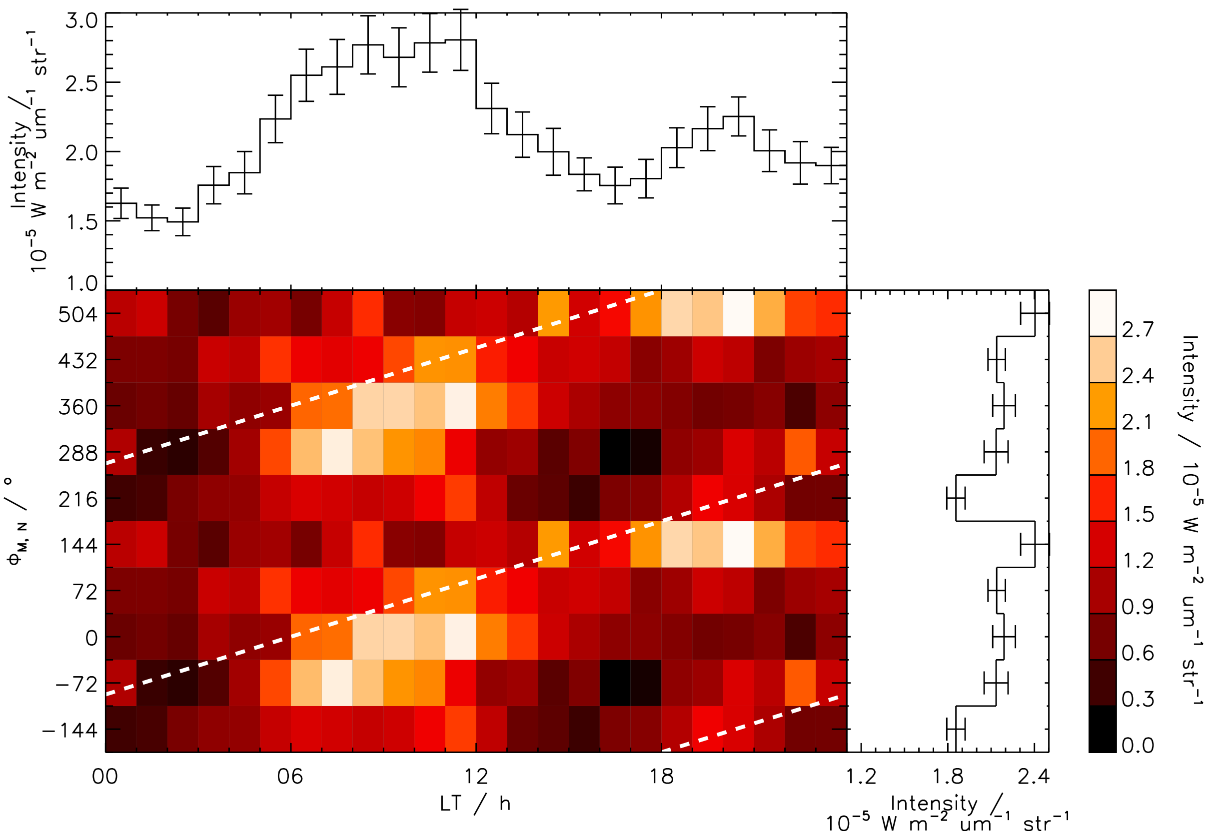

Figure 4

magnetic phase. Two cycles of magnetic phase are plotted to show the continuity of the signals. There is evidence of a linear dependence of the intensity on the magnetic phase present in both the northern and southern hemisphere data. That is, the maximum intensities were not observed at a constant magnetic phase. In the northern hemisphere distribution, where more data were available, there is less scatter.

[23] The line plots on the right hand side of the spectrograms plot the intensities averaged across each bin of magnetic phase. The intensity is maximum at $-180° < \Phi_{M,S}(t) < -108°$ in the southern hemisphere, which encompasses the value $\Phi_{M,S}(t) \approx -150°$ at SKR maximum derived by *Andrews et al.* [2012], described in Section 3. Figure 4b shows that the intensity is overall maximum at $108° < \Phi_{M,N}(t) < 180°$ in the northern hemisphere, which is significantly out of phase with the value derived for northern SKR maximum, $\Phi_{M,N} \approx 0°$, described in Section 3.

[24] In each spectrogram panel of Figure 4 the expected location of the maximum upward field-aligned current is plotted by the dashed white lines. From the definitions above, this line passes through azimuth $\phi_{U,S} = \Phi_{M,S} + 90°$ in the southern hemisphere and $\phi_{U,N} = \Phi_{M,N} - 90°$ in the northern hemisphere (remembering that ϕ is azimuthal angle referenced to noon, such that in general local time is related to ϕ by LT = $[(\phi + 180) \bmod 360]/15$). In both the northern and southern data, the maximum intensities follow the sense of this line, moving through ~24 h of LT (360° azimuth) in each 360° of magnetic phase.

[25] Although the regions of maximum emission intensity follow the slope of the lines indicating the maximum upward current region, the peak intensities are offset to later LT, particularly for the northern hemisphere data. This suggests that the peak IR intensity is slightly displaced from the peak upward current location defined by the magnetic phase model.

[26] To examine this displacement, the intensity dependence on 'magnetic longitude' has been considered. This is a rotating longitude system, referenced only to the direction of the effective dipole. The magnetic longitude of an auroral feature located at azimuth ϕ is defined by $\Phi_{M,N/S} - \phi$. This longitude system then excludes the local time variation of the intensity distributions. For example, using the relations defined above, the model upward field-aligned current is maximum at a magnetic longitude of $\Phi_{M,S} - \phi_{U,S} = -90°$ in the southern hemisphere and $\Phi_{M,N} - \phi_{U,N} = +90°$ in the northern hemisphere (see Figure 2).

[27] The resulting distributions are plotted in Figures 5a and 5b, for the south and north, respectively, in the same format as Figure 4, minus the LT distributions. The histograms in the right hand panels show the average intensities in each magnetic longitude bin and the associated standard errors. On each of these a model sinusoid is also plotted in red, indicating the intensity of the model rotating upward field-aligned current system, normalized to the peak IR intensity in each case. As just stated, the model upward field-aligned current is maximum (represented by sinusoid maximum) at $\Phi_{M,S} - \phi_{U,S} = -90°$ in the southern hemisphere and $\Phi_{M,N} - \phi_{U,N} = +90°$ in the northern hemisphere.

[28] The southern hemisphere distribution, in Figure 5a, shows horizontal banding in the color spectrogram and a peak in the histogram, indicating that the H_3^+ emission intensity is well organized by southern magnetic longitude, $\Phi_{M,S} - \phi$. That is, the intensity maximizes at a particular azimuthal separation from the model effective dipole direction. It exhibits a clear maximum at $180° < \Phi_{M,S} - \phi < 252°$ and decreases to a minimum 180° either side of this. The grey line plots a sinusoidal fit to the data averaged over 40°-wide bins of magnetic longitude. The maxima of the fit are displaced from those of the modelled upward field-aligned current sinusoid by ~−70 ± 20°. The ranges of magnetic longitude quoted obviously depend on the width of the longitude bins used, where the minimum width equivalent to the longest VIMS image integration time (40° ≈ 70 min) has been used here to determine the sinusoidal fit.

[29] The northern hemisphere intensity distribution, plotted in Figure 5b is also well organized by the northern magnetic longitude, $\Phi_{M,N} - \phi$. The maximum intensity occurs at $\Phi_{M,N} - \phi \sim 0°$, and the minima at 180° either side. In this case the peak of the sinusoidal fit to the distribution (grey) is displaced from the model sinusoid (red) by ~−80 ± 20°.

[30] We finally consider whether the northern IR intensities can be organized by the southern magnetic phase, which was the dominant signal in the magnetic field oscillations during this pre-equinox interval [*Provan et al.*, 2011], and vice versa. In Figure 5d the distribution of the northern hemisphere intensities is plotted versus southern magnetic longitude $\Phi_{M,S} - \phi$. Comparison of this distribution with that in Figure 5b shows that while there is some organization still present, the distribution is broader with a lower peak. The distribution is 180° out of phase with the southern intensity distribution shown in Figure 5a, and its peak is significantly shifted by ~115° from that of the modelled southern field-aligned current (red line).

[31] The southern intensities are similarly plotted as a function of the northern magnetic longitude $\Phi_{M,N} - \phi$ in Figure 5c. The intensities show a weak dependence on the northern phase, with maxima and minima around 0° and ±180°, which are the same values as for the northern intensities, and again are displaced from the model sinusoid peaks by ~130°.

6. Discussion

[32] The distributions in Figure 4 show that the H_3^+ emission exhibits strong local time dependencies in both hemispheres,

Figure 4. Maximum IR auroral intensities as functions of local time (in 1 h bins) and magnetic phase (72° bins). (a) Intensities derived from 33 images of the southern hemisphere as a function of southern magnetic phase, $\Phi_{M,S}$. Two phase cycles are plotted for clarity. Grey shading indicates where no data were obtained. The line plots in the top and right hand panels show the average intensities across each bin of local time and magnetic phase, respectively. The error bars indicate the standard errors of the values in each LT or phase bin. (b) Same layout as Figure 4a but for intensities derived from 78 northern hemisphere images plotted as a function of northern magnetic phase, $\Phi_{M,N}$.

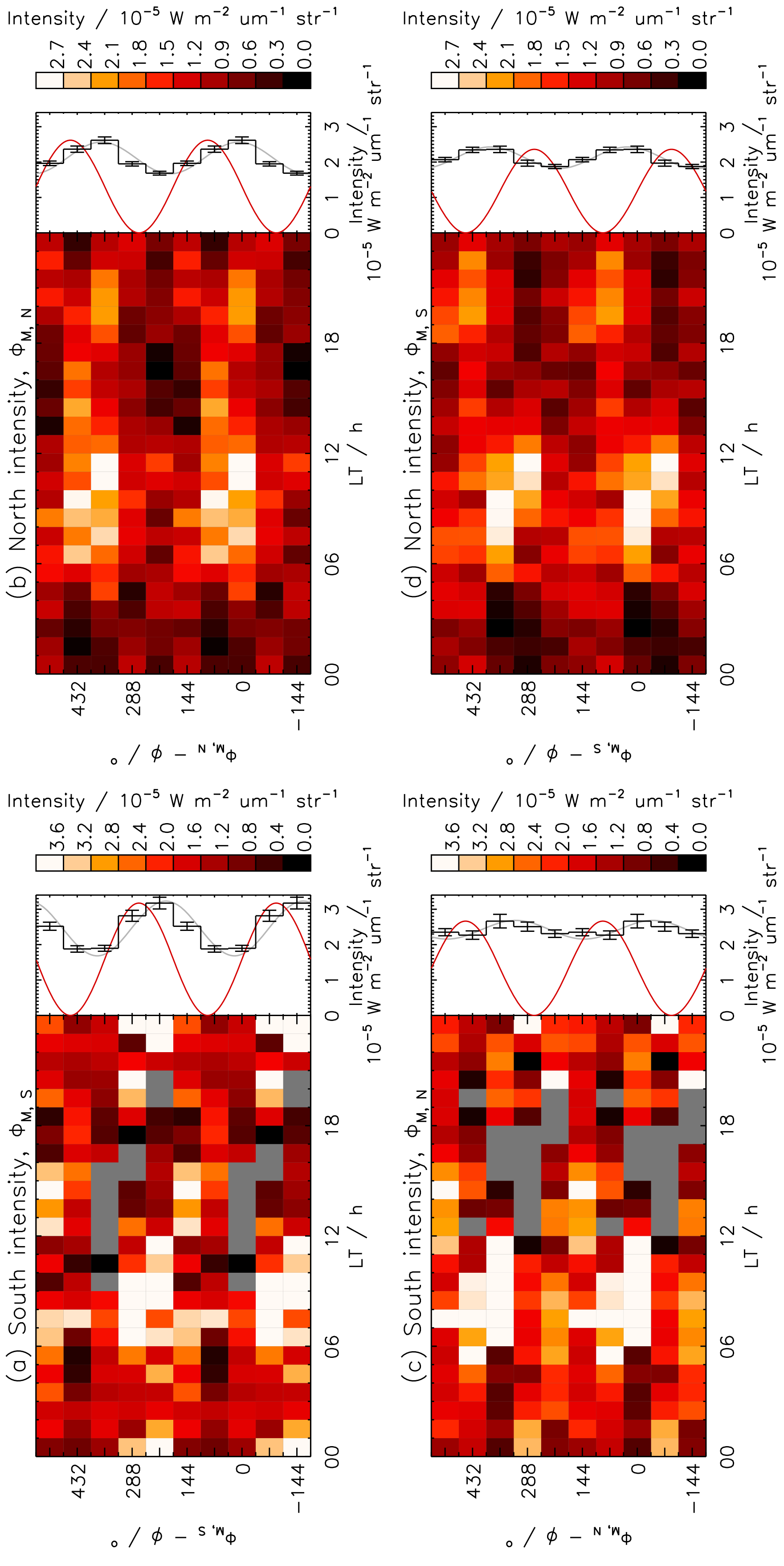
(a) South intensity, $\Phi_{M,S}$
(b) North intensity, $\Phi_{M,N}$
(c) South intensity, $\Phi_{M,N}$
(d) North intensity, $\Phi_{M,S}$
$\Phi_{M,S} - \phi$ / °
$\Phi_{M,N} - \phi$ / °
432
288
144
0
−144
LT / h
00
06
12
18
Intensity / 10^{-5} W m^{-2} um^{-1} str^{-1}
0
1
2
3
3.6
3.2
2.8
2.4
2.0
1.6
1.2
0.8
0.4
0.0
2.7
2.4
2.1
1.8
1.5
1.2
0.9
0.6
0.3
0.0

Figure 5

with maxima post-dawn and minima around dusk. Additionally, there is evidence of a rotational dependence of H_3^+ emission intensity in both hemispheres, as the region of maximum intensity moves through ~24 h of LT (360° azimuth) in each 360° of magnetic phase. This demonstrates that the intensity is related to the azimuthal rotation of the upward field-aligned current system in each hemisphere.

6.1. Field-Aligned Current Distributions

[33] For a constant, rotating source of auroral emission, the average intensity would be the same at all LT. The LT profiles displayed in Figure 4 show that this is not the case. In both hemispheres, the maximum intensity occurs in the post-dawn regions. A minimum in intensity is observed around dusk, before a second increase in intensity occurs post-dusk to midnight. This behavior is clearer in the northern hemisphere data, where more images were available, but is also apparent in the noisier southern hemisphere data.

[34] A possible interpretation of this LT profile invokes the superposition of two field-aligned current systems; one rotating and one fixed in LT. The latter is associated with the solar wind interaction, which causes sweep-back of the magnetic field lines in the outer magnetosphere. The solar wind interaction with Saturn's magnetosphere is not yet fully understood but could be caused by either a Dungey-cycle type interaction, or viscous processes, or a combination of the two, depending on the solar wind and interplanetary magnetic field (IMF) conditions.

[35] In the former interaction, circulation in the outer magnetosphere is driven by reconnection with the IMF at the dayside magnetopause to form anti-sunward moving open field lines, which subsequently close via reconnection in the tail current sheet [*Dungey*, 1961]. Large flux transfer events, like those which occur at the Earth's magnetopause, have not been observed at Saturn, however, evidence for reconnection has been identified in the form of a normal component of the magnetic field and heated or mixed magnetosphere-magnetosheath electron populations at the magnetopause [*Huddleston et al.*, 1997; *McAndrews et al.*, 2008; *Lai et al.*, 2012]. *Lai et al.* [2012] concluded that these 'connected' flux tubes could maintain Saturn's open polar caps even though the flux transport in the sub-solar region is small. A shear exists between the anti-sunward open field lines at highest latitudes and the sub-corotating, outermost closed field lines at adjacent lower latitudes [*Cowley et al.*, 2004b].

[36] Alternatively, viscous processes at the magnetopause boundary can cause coupling with the solar wind, for example via the Kelvin-Helmholtz instability. Evidence for growth of the Kelvin-Helmholtz instability at Saturn's magnetopause has been presented in Cassini data and simulations [e.g., *Masters et al.*, 2009; *Delamere et al.*, 2011]. Viscous coupling can again cause anti-sunward dragging of planetary field lines in the outer magnetosphere, leading to a shear in the magnetic field in the outer magnetosphere.

[37] Both of these processes can include local time asymmetries, due to the sub-corotational flows relative to the sheath flow at the dawn and dusk sides of the boundary. The Vasyliunas-cycle, in which mass-loaded, closed field lines become stretched down the dusk flank of the magnetosphere until reconnection occurs to release a plasmoid downtail, and the mass-depleted planetary field line contracts and rotates toward the dawnside magnetosphere, may also contribute to the LT-asymmetry of the field in the outer magnetosphere [*Vasyliunas*, 1983].

[38] As a result of the solar wind-induced magnetic shear across the outer magnetosphere, a field-aligned current flows. The current is directed upward from the planet on the dawnside of both hemispheres and downward toward the planet on the duskside of both hemispheres. The sign of the swept-back field reverses at the equator, therefore the sign of the field-aligned current also reverses there. This quasi-static, LT-asymmetric current system and its interaction with a rotating field-aligned current have been suggested by *Southwood and Kivelson* [2009] to explain the dawn-dusk asymmetry in the SKR emitted power.

[39] The interaction of an LT-fixed, field-aligned current system with a rotating current system could explain the LT distribution of the H_3^+ emission intensity observed in Figure 4. As the rotating upward current sweeps through the post-dawn sector, it reinforces the LT-fixed upward current in that region leading to a maximum current (and hence auroral intensity) in this sector. When the rotating upward current region passes toward dusk, the net upward current is reduced because of the supposed quasi-static downward current present. As the rotating system continues toward midnight the downward current decreases and the net upward current increases again. This sequence explains the overall auroral intensity maxima post-dawn and the minima around dusk seen in Figures 4a and 4b.

[40] The northern hemisphere intensities also demonstrated a weaker modulation by the southern hemisphere magnetic phase (Figure 5d). The northern intensity maxima and minima were observed to be 180° out of phase with those of the southern hemisphere intensities. This suggests that at least part of the southern rotating field-aligned current system closed in the northern hemisphere, i.e. a region of upward current (intense auroral emission) in the southern hemisphere corresponded to a region of downward current (weaker or no auroral emission) in the northern hemisphere.

[41] A system of inter-hemispheric field-aligned currents was proposed by *Southwood and Kivelson* [2007] to explain the magnetic field oscillations, however, their model used only one current system rotating at a single period, which

Figure 5. Average IR intensities organized according to magnetic longitude in the same format as Figure 4. (a) Southern intensities organized by $\Phi_{M,S} - \phi$. (b) Northern intensities organized by $\Phi_{M,N} - \phi$. (c) Southern intensities organized by $\Phi_{M,N} - \phi$. (d) Northern intensities organized by $\Phi_{M,S} - \phi$. The histograms in the right hand panels show the average intensities across each bin of magnetic longitude. The error bars indicate the standard errors of the values in each magnetic longitude bin. The grey lines plot a sinusoidal fit to the data averaged over 40° bins of longitude. The red lines plot a model sinusoid function, scaled to the maximum intensity of each distribution. The maximum upward field-aligned currents (the peaks of the model sinusoid) are expected at $\Phi_{M,S} - \phi = -90°$ for the southern system and $\Phi_{M,N} - \phi = +90°$ for the northern system.

does not account for the separate northern and southern periods later identified. To explain the suggestion of currents partially closing in the opposite hemisphere, both this model and that of *Andrews et al.* [2010], illustrated in Figure 1, require some modification. The southern intensities display a weak modulation by the northern magnetic phase, in phase with that of the northern intensities, although the effect may not be particularly significant given the noisiness of the data represented by the error bars in Figure 5c.

[42] While the auroral intensities are modulated by the magnetic phases systems as just described, the locations of the peaks and troughs do not exactly match those predicted by the phase models. This is indicated by the offset from the model sinusoids plotted by the red lines in Figures 5a and 5b, namely $\sim -70 \pm 20°$ in the southern hemisphere and $\sim -80 \pm 20°$ in the northern hemisphere. These displacements imply that the IR intensity maximizes 3–6 h later in LT than the model upward field-aligned current. This is ahead of the maximum upward field-aligned current in the direction of planetary rotation. If the auroral emission is a direct representation of the upward current magnitude, this may suggest that the rotating field-aligned current system is not as symmetric as the simple rotating sinusoid currently modelled, as is indeed evident in the magnetic field signals used to fit the model sinusoid [*Andrews et al.*, 2012]. In this case it may reflect an earlier peak or steeper increase in the upward current profile with respect to phase than that exhibited by a strict sinusoid.

[43] The broadening of the northern intensity profile relative to the model sinusoid could be attributed to the influence of both the northern and southern current systems. A related superposition effect has been identified in the oscillations in the equatorial magnetic field data by *Provan et al.* [2011]. If part of the southern rotating field-aligned current system closes in the northern hemisphere, there will be two regions of upward current rotating with slightly different periods. This could lead to a broadening of the intensity profile and also contribute to the shift from the northern phase value where the intensity is expected to maximize.

[44] To consider possible atmospheric causes of the displacement, we note that the ionospheric H_3^+ molecules are known to travel in the sense of corotation in the brightest auroral emission regions with typical velocities of order $1\ \text{km s}^{-1}$, which is a fraction of the corotating flow velocity [*Stallard et al.*, 2007]. This is therefore too slow to account for the appearance of the maximum observed intensity 'ahead' of the maximum modelled upward current. However, other factors such as the variable ionospheric conductance and temperature also play important roles in governing the H_3^+ emission intensity. This topic requires a detailed modeling study in the future.

6.2. Comparison With Example VIMS Observation Sequence

[45] Within the restrictions imposed by the incomplete and changing FOV of the auroral region, the sequence of images shown in Figure 3 demonstrates the two dependencies of the H_3^+ auroral intensity outlined above. First, the emission was overall most intense around $\Phi_{M,N} \sim 0°$. Secondly, the most intense emissions occurred in the post-dawn sector, which, in accord with the previous statement, was close to the azimuth of the modelled maximum upward current at that time. The converse behavior is also observed: dimmer aurora at $\Phi_{M,N} \sim 180°$ and on the dusk side.

[46] In general the most intense emission occurred at later LT than the maximum upward current from the model, further exemplifying the trend seen in Figure 4b. Consideration of the superposition of the LT-fixed and rotating current systems reveals that the point of maximum upward current (and auroral intensity) first appears ahead of the peak of the rotating system, as the rotating profile sweeps over the rising portion of the LT-fixed profile, and then appears to lag the rotating peak as it sweeps over the declining profile of the LT-fixed system. Overall this would be observed as a sub-corotating intense auroral feature. There is evidence of this effect in Figures 3e and 3f, as the upward field-aligned current reference axis (yellow line) sweeps across the most intense patch of aurora toward local noon, implying the current system is rotating faster than the most intense auroral region.

[47] It is important to note that the profile of the 'LT-fixed' current system could in fact be variable, depending on the solar wind conditions, as has been suggested to explain the variation of the southern SKR period on timescales of weeks by *Zarka et al.* [2007]. Furthermore, the reference magnetic phase system employed does not reflect possible variations in phase on timescales shorter than 200 days [*Andrews et al.*, 2012], such that the possibility of a sampling bias acquired through the auroral images cannot be excluded. There may also be considerable variability imposed by the occurrence of sub-corotating auroral 'blobs' such as those seen here and previously identified by *Grodent et al.* [2005], which may be related to dynamic magnetospheric processes which can occur independent of the magnetic phase. These effects would be sources of uncertainty in analyzing the LT and phase dependencies over long timescales.

7. Summary

[48] This study has examined the rotational modulation and local time dependence of Saturn's pre-equinoctial H_3^+ auroral intensity. The intensity distributions in each hemisphere were modulated by the corresponding magnetic phase systems, which define the rotation of a field-aligned current system in each hemisphere. However, the maxima in auroral intensity were out of phase with the expected maxima of the upward field-aligned current in each hemisphere, occurring ahead of the expected maxima in the upward current in the direction of planetary rotation, i.e. at later LT. This may indicate that the rotating current system may be more complex and asymmetric than the simple sinusoid employed in the model.

[49] The aurorae in both hemispheres were on average more intense in the post-dawn sector. The LT width of the peak in the northern hemisphere was noticeably broader than that in the southern hemisphere. Reduced intensities were observed around dusk and post-midnight in both hemispheres. The LT variation of the auroral intensity can be explained by the superposition of the rotating current system with a quasi-static field-aligned current system associated with the solar wind interaction. This latter current is expected to be directed upward at dawn and downward at dusk in both hemispheres, thereby enhancing the rotating upward field-aligned auroral current when it passes through the dawn sector and reducing it around dusk.

[50] The LT profile observed is consistent with long-term (2004 and 2007) observations of LT asymmetries in the southern SKR and UV emission intensities [e.g., *Lamy et al.*, 2009]. However, recent analysis by *Carbary* [2012] of UV auroral observations made during 2007–2009 has shown that the statistical peak in UV emission occurred earlier at around 5 LT in both hemispheres. They suggested that this shift to earlier LT could be caused by a seasonal change in high-altitude zonal winds affecting the field-aligned current systems. This shift is not observed in the IR emissions analyses in the present study, which cover approximately the same epoch, suggesting that the IR (H_3^+) and UV (H and H_2) emissions may not identically reflect the auroral field-aligned current profile (i.e. its intensity) because of other influences such as thermospheric temperature [e.g., *Tao et al.*, 2011]. This comparison and its relationship to the field-aligned current profile remains to be clarified, but could contribute to the observed phase offset.

[51] The northern intensities also displayed weak modulation by the southern phase system, ~180° out of phase with the southern intensities, indicating the partial closure of the rotating currents between the two hemispheres [*Southwood and Kivelson*, 2007]. This could lead to a broadening in LT and offset in phase of the intensity profile. A less significant modulation of the southern intensities by the northern phase, in phase with that of the northern intensities was also present.

[52] The dependencies found are revealed by statistical analysis of a large number of auroral images, while part of the identified variability can be attributed to variability of the 'LT-fixed' current profile related to the solar wind interaction, and auroral features resulting from phase-independent magnetospheric dynamics. A comparative analysis of UV auroral emissions from H and H_2 should isolate whether the broadened northern LT profile and offset of the maximum intensity are unique to the H_3^+ aurora, and help establish the influence of atmospheric chemistry on the observed patterns. It will be interesting to analyze observations of the post-equinox aurora to observe additional sequences of auroral dynamics and see how the overall behavior changes with planetary season. Such tracking of the current systems will contribute to understanding the underlying rotation of the planetary field and deep interior.

[53] **Acknowledgments.** DJA was supported by an SNSP grant. Work at Leicester was supported by STFC grants ST/H002480/1 and ST/G002223/1.

[54] Robert Lysak thanks the reviewers for their assistance in evaluating this paper.

References

Andrews, D. J., E. J. Bunce, S. W. H. Cowley, M. K. Dougherty, G. Provan, and D. J. Southwood (2008), Planetary period oscillations in Saturn's magnetosphere: Phase relation of equatorial magnetic field oscillations and Saturn kilometric radiation modulation, *J. Geophys. Res.*, *113*, A09205, doi:10.1029/2007JA012937.

Andrews, D. J., A. J. Coates, S. W. H. Cowley, M. K. Dougherty, L. Lamy, G. Provan, and P. Zarka (2010), Magnetospheric period oscillations at Saturn: Comparison of equatorial and high-latitude magnetic field periods with north and south Saturn kilometric radiation periods, *J. Geophys. Res.*, *115*, A12252, doi:10.1029/2010JA015666.

Andrews, D. J., S. W. H. Cowley, M. K. Dougherty, L. Lamy, G. Provan, and D. J. Southwood (2012), Planetary period oscillations in Saturn's magnetosphere: Evolution of magnetic oscillation properties from southern summer to post-equinox, *J. Geophys. Res.*, *117*, A04224, doi:10.1029/2011JA017444.

Badman, S. V., N. Achilleos, K. H. Baines, R. H. Brown, E. J. Bunce, M. K. Dougherty, H. Melin, J. D. Nichols, and T. Stallard (2011a), Location of Saturn's northern infrared aurora determined from Cassini VIMS images, *Geophys. Res. Lett.*, *38*, L03102, doi:10.1029/2010GL046193.

Badman, S. V., C. Tao, A. Grocott, S. Kasahara, H. Melin, R. H. Brown, K. H. Baines, M. Fujimoto, and T. Stallard (2011b), Cassini VIMS observations of latitudinal and hemispheric variations in Saturn's infrared auroral intensity, *Icarus*, *216*, 367–375, doi:10.1016/j.icarus.2011.09.031.

Brown, R. H., et al. (2004), The Cassini Visual and Infrared Mapping Spectrometer (VIMS) investigation, *Space Sci. Rev.*, *115*(1–4), 111–168, doi:10.1007/s11214-004-1453-x.

Carbary, J. F. (2012), The morphology of Saturn's ultraviolet aurora, *J. Geophys. Res.*, *117*, A06210, doi:10.1029/2012JA017670.

Carbary, J. F., S. M. Krimigis, D. G. Mitchell, C. Paranicas, and P. Brandt (2009), Energetic neutral atom (ENA) and charged particle periodicities in Saturn's magnetosphere, *Adv. Space Res.*, *44*, 483–493, doi:10.1016/j.asr.2009.04.019.

Cowley, S. W. H., E. J. Bunce, and J. M. O'Rourke (2004a), A simple quantitative model of plasma flows and currents in Saturn's polar ionosphere, *J. Geophys. Res.*, *109*, A05212, doi:10.1029/2003JA010375.

Cowley, S. W. H., E. J. Bunce, and R. Prange (2004b), Saturn's polar ionospheric flows and their relation to the main auroral oval, *Ann. Geophys.*, *22*(4), 1379–1394.

Delamere, P. A., R. J. Wilson, and A. Masters (2011), Kelvin-Helmholtz instability at Saturn's magnetopause: Hybrid simulations, *J. Geophys. Res.*, *116*, A10222, doi:10.1029/2011JA016724.

Desch, M. D., and M. L. Kaiser (1981), Voyager measurement of the rotation period of Saturn's magnetic field, *Geophys. Res. Lett.*, *8*, 253–256, doi:10.1029/GL008i003p00253.

Drossart, P., et al. (1989), Detection of H_3^+ on Jupiter, *Nature*, *340*, 539–541.

Dungey, J. W. (1961), Interplanetary magnetic field and the auroral zones, *Phys. Res. Lett.*, *6*, 47–48, doi:10.1103/PhysRevLett.6.47.

Espinosa, S. A., and M. K. Dougherty (2000), Periodic perturbations in Saturn's magnetic field, *Geophys. Res. Lett.*, *27*, 2785–2788, doi:10.1029/2000GL000048.

Galand, M., L. Moore, I. Mueller-Wodarg, M. Mendillo, and S. Miller (2011), Response of Saturn's auroral ionosphere to electron precipitation: Electron density, electron temperature, and electrical conductivity, *J. Geophys. Res.*, *116*, A09306, doi:10.1029/2010JA016412.

Galopeau, P. H. M., and A. Lecacheux (2000), Variations of Saturn's radio rotation period measured at kilometer wavelengths, *J. Geophys. Res.*, *105*, 13,089–13,102, doi:10.1029/1999JA005089.

Grodent, D., J.-C. Gérard, S. W. H. Cowley, E. J. Bunce, and J. T. Clarke (2005), Variable morphology of Saturn's southern ultraviolet aurora, *J. Geophys. Res.*, *110*, A07215, doi:10.1029/2004JA010983.

Gurnett, D. A., et al. (2004), The Cassini radio and plasma wave investigation, *Space Sci. Rev.*, *114*, 395–463, doi:10.1007/s11214-004-1434-0.

Gurnett, D. A., A. Lecacheux, W. S. Kurth, A. M. Persoon, J. B. Groene, L. Lamy, P. Zarka, and J. F. Carbary (2009), Discovery of a north-south asymmetry in Saturn's radio rotation period, *Geophys. Res. Lett.*, *36*, L16102, doi:10.1029/2009GL039621.

Huddleston, D. E., C. T. Russell, G. Le, and A. Szabo (1997), Magnetopause structure and the role of reconnection at the outer planets, *J. Geophys. Res.*, *102*, 24,289–24,302, doi:10.1029/97JA02416.

Kaiser, M. L., M. D. Desch, J. W. Warwick, and J. B. Pearce (1980), Voyager detection of nonthermal radio emission from Saturn, *Science*, *209*, 1238–1240, doi:10.1126/science.209.4462.1238.

Kurth, W. S., A. Lecacheux, T. F. Averkamp, J. B. Groene, and D. A. Gurnett (2007), A Saturnian longitude system based on a variable kilometric radiation period, *Geophys. Res. Lett.*, *34*, L02201, doi:10.1029/2006GL028336.

Lai, H. R., H. Y. Wei, C. T. Russell, C. S. Arridge, and M. K. Dougherty (2012), Reconnection at the magnetopause of Saturn: Perspective from FTE occurrence and magnetosphere size, *J. Geophys. Res.*, *117*, A05222, doi:10.1029/2011JA017263.

Lamy, L. (2011), Variability of southern and northern periodicities of Saturn Kilometric Radiation, in *Planetary Radio Emissions*, edited by H. O. Rucker, pp. 39–50, Austrian Acad. Sci. Press, Vienna, doi:10.1553/PRE7s39.

Lamy, L., B. Cecconi, R. Prangé, P. Zarka, J. D. Nichols, and J. T. Clarke (2009), An auroral oval at the footprint of Saturn's kilometric radio sources, colocated with the UV aurorae, *J. Geophys. Res.*, *114*, A10212, doi:10.1029/2009JA014401.

Masters, A., N. Achilleos, C. Bertucci, M. K. Dougherty, S. J. Kanani, C. S. Arridge, H. J. McAndrews, and A. J. Coates (2009), Surface waves on Saturn's dawn flank magnetopause driven by the Kelvin-Helmholtz instability, *Planet. Space. Sci.*, *57*, 1769–1778, doi:10.1016/j.pss.2009.02.010.

McAndrews, H. J., C. J. Owen, M. F. Thomsen, B. Lavraud, A. J. Coates, M. K. Dougherty, and D. T. Young (2008), Evidence for reconnection at Saturn's magnetopause, *J. Geophys. Res.*, *113*, A04210, doi:10.1029/2007JA012581.

Melin, H., T. Stallard, S. Miller, J. Gustin, M. Galand, S. V. Badman, W. R. Pryor, J. O'Donoghue, R. H. Brown, and K. H. Baines (2011), Simultaneous Cassini VIMS and UVIS observations of Saturn's southern aurora: comparing emissions from H, H_2 and H_3^+ at a high spatial resolution, *Geophys. Res. Lett.*, *38*, L15203, doi:10.1029/2011GL048457.

Mitchell, D. G., J. F. Carbary, S. W. H. Cowley, T. W. Hill, and P. Zarka (2009), The dynamics of Saturn's magnetosphere, in *Saturn From Cassini-Huygens*, edited by M. K. Dougherty, L. W. Esposito, and S. M. Krimigis, pp. 257–280, Springer, Dordrecht, Netherlands, doi:10.1007/978-1-4020-9217-6.

Nichols, J. D., J. T. Clarke, S. W. H. Cowley, J. Duval, A. J. Farmer, J.-C. Gérard, D. Grodent, and S. Wannawichian (2008), Oscillation of Saturn's southern auroral oval, *J. Geophys. Res.*, *113*, A11205, doi:10.1029/2008JA013444.

Nichols, J. D., B. Cecconi, J. T. Clarke, S. W. H. Cowley, J.-C. Gérard, A. Grocott, D. Grodent, L. Lamy, and P. Zarka (2010a), Variation of Saturn's UV aurora with SKR phase, *Geophys. Res. Lett.*, *37*, L15102, doi:10.1029/2010GL044057.

Nichols, J. D., S. W. H. Cowley, and L. Lamy (2010b), Dawn-dusk oscillation of Saturn's conjugate auroral ovals, *Geophys. Res. Lett.*, *37*, L24102, doi:10.1029/2010GL045818.

Provan, G., D. J. Andrews, C. S. Arridge, A. J. Coates, S. W. H. Cowley, S. E. Milan, M. K. Dougherty, and D. M. Wright (2009), Polarization and phase of planetary-period magnetic field oscillations on high-latitude field lines in Saturn's magnetosphere, *J. Geophys. Res.*, *114*, A02225, doi:10.1029/2008JA013782.

Provan, G., D. J. Andrews, B. Cecconi, S. W. H. Cowley, M. K. Dougherty, L. Lamy, and P. M. Zarka (2011), Magnetospheric period magnetic field oscillations at Saturn: Equatorial phase "jitter" produced by superposition of southern and northern period oscillations, *J. Geophys. Res.*, *116*, A04225, doi:10.1029/2010JA016213.

Sandel, B. R., et al. (1982), Extreme ultraviolet observations from the Voyager 2 encounter with Saturn, *Science*, *215*, 548–553, doi:10.1126/science.215.4532.548.

Southwood, D. (2011), Direct evidence of differences in magnetic rotation rate between Saturn's northern and southern polar regions, *J. Geophys. Res.*, *116*, A01201, doi:10.1029/2010JA016070.

Southwood, D. J., and M. G. Kivelson (2007), Saturnian magnetospheric dynamics: Elucidation of a camshaft model, *J. Geophys. Res.*, *112*, A12222, doi:10.1029/2007JA012254.

Southwood, D. J., and M. G. Kivelson (2009), The source of Saturn's periodic radio emission, *J. Geophys. Res.*, *114*, A09201, doi:10.1029/2008JA013800.

Stallard, T., C. Smith, S. Miller, H. Melin, M. Lystrup, A. Aylward, N. Achilleos, and M. K. Dougherty (2007), Saturn's auroral/polar H_3^+ infrared emission-II. A comparison with plasma flow models, *Icarus*, *191*(2), 678–690, doi:10.1016/j.icarus.2007.05.016.

Stallard, T. S., H. Melin, S. Miller, S. V. Badman, R. H. Brown, and K. H. Baines (2012), Peak emission altitude of Saturn's H_3^+ aurora, *Geophys. Res. Lett.*, *39*, L15103, doi:10.1029/2012GL052806.

Tao, C., S. V. Badman, and M. Fujimoto (2011), UV and IR auroral emission model for the outer planets: Jupiter and Saturn comparison, *Icarus*, *213*, 581–592, doi:10.1016/j.icarus.2011.04.001.

Vasyliunas, V. M. (1983), Plasma distribution and flow, in *Physics of the Jovian Magnetosphere*, edited by A. J. Dessler, pp. 395–453, Cambridge Univ. Press, New York.

Zarka, P., L. Lamy, B. Cecconi, R. Prangé, and H. O. Rucker (2007), Modulation of Saturn's radio clock by solar wind speed, *Nature*, *450*, 265–267, doi:10.1038/nature06237.